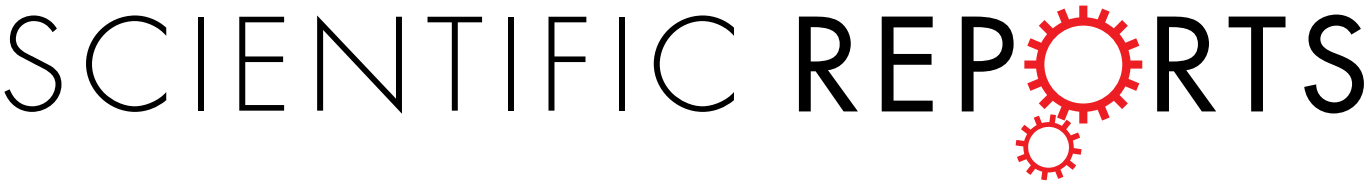

OPEN

Templating synthesis of Fe_2O_3 hollow spheres modified with Ag nanoparticles as superior anode for lithium ion batteries

Received: 30 March 2017
Accepted: 18 July 2017
Published online: 29 August 2017

Xiaoping Lin, Jianmin Zhang, Xiaobin Tong, Han Li, Xi Pan, Peigong Ning & Qiuhong Li

Ag-Fe_2O_3 hollow spheres are synthesized by using Ag@C core-shell matrix as sacrificial templates. The morphologies and structures of the as-prepared samples are characterized by scanning electron microscopy, X-ray powder diffraction energy dispersive, transmission electron microscopy and high resolution transmission electron microscopy. In contrast to Fe_2O_3 hollow spheres, Ag-Fe_2O_3 hollow spheres exhibit much higher electrochemical performances. The Ag-Fe_2O_3 composites exhibit an initial discharge capacity of 1030.9 mA h g^{-1} and retain a high capacity of 953.2 mA h g^{-1} at a current density of 100 mA g^{-1} after 200 cycles. Furthermore, Ag-Fe_2O_3 electrode can maintain a stable capacity of 678 mA h g^{-1} at 1 A g^{-1} after 250 cycles. Rate performance of Ag-Fe_2O_3 electrode exhibits a high capacity of 650.8 mA h g^{-1} even at 5 A g^{-1}. These excellent performances can be attributed to the decoration of Ag particles which will enhance conductivity and accelerate electrochemical reaction kinetics. Moreover, the hollow structure and the constructing particles with nanosize will benefit to accommodate huge volume change and stabilize the structure.

In recent decades, a lot of studies had been triggered in developing high-performance electrode materials with high energy density, high power density, long lifetime and low cost[1–4]. Since the first report by Tarascon *et al.*[5], transition metal oxides (TMOs) had been identified as promising candidates for lithium ion batteries due to their low conversion potential, high specific capacity and environmental friendliness[6–10]. Among the TMOs, Fe_2O_3 was considered as a promising anode for lithium ion batteries (LIBs) because of its low cost, high theoretical capacity (1007 mA h g^{-1}), environmental protection and nontoxicity[11–13]. As evidenced by countless research works, the high capacity was mainly obtained by the reversible conversion reaction between Fe_2O_3 and Li^+ [14]. Recently, there had been a great deal of progress in the study of Fe_2O_3 based electrode material[15–18]. Lou *et al.* fabricated carbon-coated α- Fe_2O_3 hollow nanohorns on the CNT backbone, which greatly improved the electrochemical properties of Fe_2O_3 electrode[16]. However, the commercial applications of Fe_2O_3 in LIBs were impeded by the sluggish conversion reactions, large volume expansion and contraction during the charge and discharge cycles[19]. Two strategies had been developed to overcome these significant drawbacks. One was to retain a large deal of void space by synthesizing porous/nanostructured anode materials (e.g. nanotubes[20, 21], mesoporous materials[22, 23], nanopeapods[24]), which presented to accommodate the volume change and shorten the Li^+ transport distance. Thus, they could exhibit enhanced rate capability and improved cycle retention[25]. Another was to coat native materials with carbon[26] or decorate some conductive materials to increase the electrical conductivity and alleviate aggregation[27–29]. Kim *et al.* fabricated Ag-$Li_4Ti_5O_{12}$ nanofibers by electrospinning, which displayed enhanced rate capability and cycling stability compared to the bare $Li_4Ti_5O_{12}$[28]. To the best of our knowledge, a hollow structure of Fe_2O_3 nanospheres decorated with Ag nanoparticles had never been reported, and we expected the introduction of Ag could improve the electrochemical properties of Fe_2O_3.

In recent years, template-based method was widely used in preparing hollow nanostructured materials[30–32]. In this work, we successfully synthesized Ag-Fe_2O_3 hollow nanospheres by using Ag@C core-shell matrix as sacrificial templates. The removal of carbon layer and surface diffusion during the annealing process was the main reason for the formation of hollow nanostructures. As the temperature up to 600 °C, Ag core started to melted and partial hollow core formed[33]. Ag-Fe_2O_3 composites displayed a unique hollow structure which obviously

Pen-Tung Sah Institute of Micro-Nano Science and Technology, Xiamen University, Xiamen, 361005, China. Correspondence and requests for materials should be addressed to Q.L. (email: liqiuhong@xmu.edu.cn)

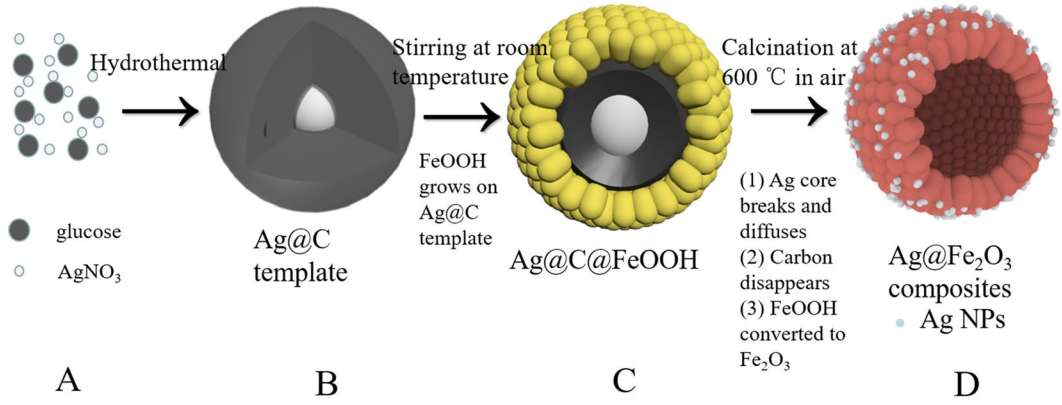

Figure 1. Schematic illustration of a tentative mechanism for the template-directed synthesis of the Ag decorated Fe_2O_3 nanospheres.

shortened the Li^+ transport distance and effectively slowed down the volume expansion. The incorporation of Ag could effectively improve the conductivity of the material. Compared with Fe_2O_3 hollow nanospheres, Ag-Fe_2O_3 hollow nanospheres displayed enhanced cycling properties and excellent performance at high rates.

Results and Discussions

The schematic illustration of a tentative mechanism for the template-directed synthesis of the Ag modified Fe_2O_3 nanospheres is shown in Fig. 1. Initially, we synthesize Ag@C templates by hydrothermal method (A → B). Then, Ag@C templates are coated with FeOOH by stirring at room temperature (B → C). In the course of stirring, CH_3COO^- hydrolysis to produce OH^-, then, Fe^{2+} react with OH^- and O_2, and ultimately form FeOOH ($CH_3COO^- + H_2O \rightarrow CH_3COOH + OH^-$, $4Fe^{2+} + 8OH^- + O_2 \rightarrow 4FeOOH + 2H_2O$).Next, during the calcinations at air (C → D), with the disappearance of carbon layer, Ag core breaks and diffuses, in the meantime, FeOOH converts to Fe_2O_3. Eventually, Ag-Fe_2O_3 hollow spheres are fabricated. The formation of Fe_2O_3 hollow structure decorated with Ag nanoparticles can be related with the removal of carbon template and surface diffusion processes. During the annealing, along with the disappearance of the carbon layer, Ag core begin to melt and shrink, leading to the presence of lots of Ag nanoparticle residues form inside the shell. The diffusion of the melted Ag nanoparticles takes place at the same time, which results in the formation of Fe_2O_3 hollow spheres decorated with much smaller Ag nanoparticles.

Figure 2(a) shows SEM images of the as-prepared Ag@C templates with good dispersibility and the diameter of Ag@C templates is about 650–700 nm. After the Fe_2O_3 growth and annealing procedure, Ag-Fe_2O_3 hollow spheres are obtained. As seen in Fig. 2(b,c and d), the as-synthesized Fe_2O_3 and Ag-Fe_2O_3 nanospheres are monodisperse and comparatively uniform in size. Figure 2(b) displays Fe_2O_3 nanospheres have a hollow structure. High magnification of Fe_2O_3 nanospheres inset in Fig. 2(b) reveals that the diameter of Fe_2O_3 hollow spheres is about 550 nm which is similar with Ag-Fe_2O_3. Low magnification of Ag-Fe_2O_3 shown in Fig. 2(c) indicates that the sample has more uniform morphology than Fe_2O_3. The EDS spectrum reveals that a small amount of Ag exists in the Fe_2O_3 nanospheres with the weight percentage of Ag about 3.9%. A small amount of carbon exists in Ag-Fe_2O_3 composites after annealing process, and the present of carbon is favorable to the electrochemical properties of the composite. The specific weight/atomic percentages for each element obtained from EDS measurement are given in Table S1 in supporting information (SI). High magnification of SEM illustrated in Fig. 2(d) demonstrates the diameter of Ag-Fe_2O_3 nanospheres is about 600 nm. It can also be obviously observed that Ag-Fe_2O_3 hollow nanospheres are composed of a number of Fe_2O_3 nanorods with approximately 60–70 nm long and 30–40 nm wide. Additionally, ultra-small Ag nanoparticles are evenly distributed on the surface of Fe_2O_3 spheres.

The morphology and structure of the materials are further studied by TEM, and HRTEM measurements. TEM images in Fig. 3(a and b) show Ag@C templates are uniform, each particles consists of Ag core about 150 nm in diameter and carbon shell with thickness about 230 nm. Figure 3(c) shows the Fe_2O_3 hollow spheres formed by the accumulation of Fe_2O_3 nanorods. HRTEM observations are carried out to investigate the crystalline structure. The lattice spacing shown in Fig. 3(d) are calculated to be 0.368 nm and 0.270 nm which agree with the spacing between (012) and (104) planes of α-Fe_2O_3. Figure 3(e and f) reveal Ag-Fe_2O_3 composites have a hollow structure and the wall thickness is about 60 nm. The diameter of the Ag-Fe_2O_3 nanospheres is about 600 nm, in agreement with SEM result in Fig. 2(d). Ag nanoparticles distributed on the surface of Fe_2O_3 show a size about 10 nm, much smaller than that of Ag core in Ag@C templates. This result may be due to the disintegration and diffusion of Ag core during the annealing process. Figure 3(g and h) present HRTEM images with lattice fringes take from Ag-Fe_2O_3 spheres. Figure 3(g) reveals the interlayer spacing of 0.236 nm corresponded well to the spacing of Ag (111) planes. Moreover, Fig. 3(h) indicates the lattice spacing of 0.236 nm and 0.270 nm are respectively consistent with the spacing of Ag (111) and α-Fe_2O_3 (104) planes. Figure 3(i–l) show the phase mapping of Ag Lα1, Fe Lα1 and O Lα1 tested by EDS analyzer equipped in TEM instrument, which reveal a uniform distribution of Ag elements (green) in Fe_2O_3 hollow structure.

The crystalline nature of the as-prepared Ag@C template, Fe_2O_3 nanospheres and Ag-Fe_2O_3 composites are examined by X-ray diffraction (XRD). As shown in Fig. 4, it can be seen that the diffraction peaks of Ag@C template appearing at 38.1°, 44.3°, 64.4°, 77.4° and 81.6°, which are corresponding to the cubic structure of Ag

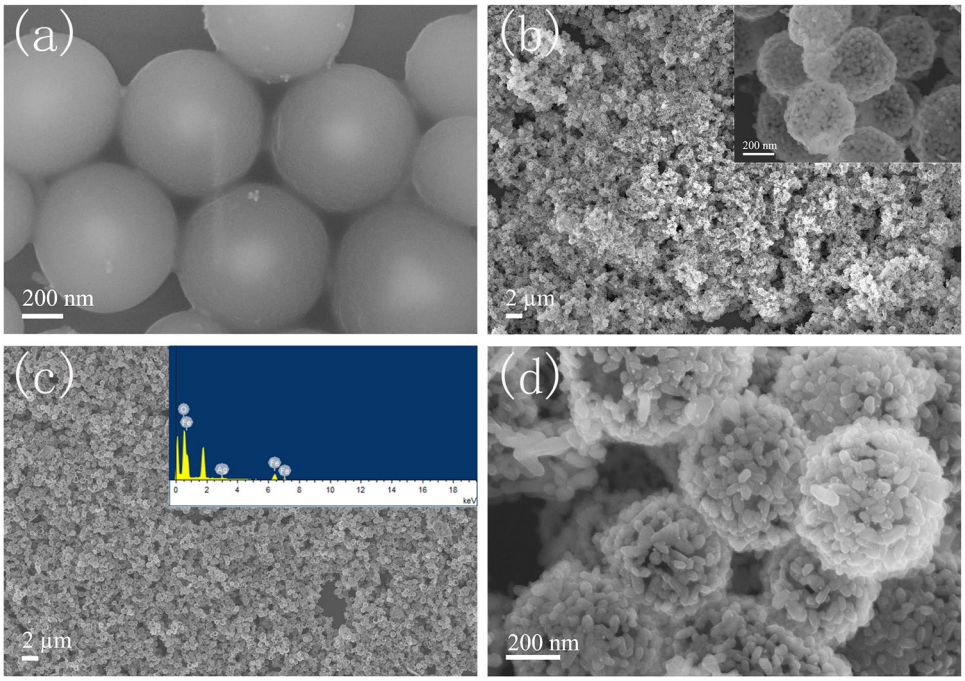

Figure 2. SEM images of the samples (**a**) Ag@C templates, (**b**) Fe_2O_3 nanospheres, (**c**) low magnification Ag-Fe_2O_3 composites and EDS spectrum of Ag-Fe_2O_3 composites, (**d**) high magnification Ag-Fe_2O_3 composites.

(JPCDS No. 89–3722). For Ag-Fe_2O_3 composites, all the diffraction peaks are indexed to the hexagonal structure of α-Fe_2O_3 phase (JCPDS No. 79–1741). The position of the diffraction peaks indicates the type of Fe_2O_3 is hematite. For better learning the type of Fe_2O_3, we also carries out Raman test. The result in Fig. S1 shows the product we obtained is hematite[34–38], in agreement with XRD results in Fig. 4. Moreover, two relatively weak peaks locate at 38.1° (111) and 44.3° (200) are discernible, which belong to the Ag nanoparticles. Fe_2O_3 nanospheres are used as a comparative sample, XRD patterns is similar to that of Ag-Fe_2O_3 composites except for the peaks of Ag. Peaks from other phases are not detected indicating high purity of the samples. The carbonaceous layer in the Ag@C templates is reducible during the high-temperature annealing process, which will protect Ag from oxidation during the diffusion process. Consequently, Ag nanoparticles are obtained in the final product rather than Ag_2O[33].

The electrochemical properties of Ag-Fe_2O_3 electrode for LIBs are systematically measured by using a lithium foil electrode as reference electrode in the coin-cell batteries. The cyclic voltammetry (CV) analysis of Ag-Fe_2O_3 electrode collect at a scan rate of 0.1 mV s^{-1} between 0.01 and 3.0 V is illustrated in Fig. 5(a). The CV curves of the sample are similar to the previously reported results[13, 39, 40]. Plenty of differences between the first cycle and consecutive cycles are noticed. At the first cycle, there are two peaks appear in the cathodic sweep. The strong reduction peak observed at 0.67 V corresponds to the reduction of Fe (III) to Fe (0) and the formation of solid-electrolyte interface (SEI), while a broad peak locate at 0.87 V can be ascribed to Li ions insertion into Fe_2O_3 without structural change as follows:

$$Fe_2O_3 + xLi^+ + xe^- \rightarrow Li_xFe_2O_3$$

During the anodic scan, two extended peaks appear at 1.64 V and 1.80 V, which is attributed to the oxidation of Fe (0) to Fe (II) and further oxidation to Fe (III)[39–41]. In subsequent cycles, the full lithiation potential is characterized by a higher voltage at 0.95 V. The change is mainly in virtue of the improved kinetics of Ag-Fe_2O_3 which can be resulted from inherent nanosize effects in the TMOs electrode during cycling. Worthy of nothing, the electrochemical behavior of the composites is largely sustained except the gradual changes in intensity or position of the peaks. These phenomena indicate the good cycling performance of Ag-Fe_2O_3 electrode. The CV curves of Fe_2O_3 nanospheres is shown in Fig. S2, which display similar electrochemical process with Ag-Fe_2O_3.

Figure 5(b) exhibits the discharge and charge voltage profiles of Ag-Fe_2O_3 electrode at a current density of 100 mA g^{-1} within a voltage window range of 0.01–3 V, which are in good agreement with the peaks of the CV curves in Fig. 5(a). A first overall discharge (lithiation) capacity is experimentally as large as 1030.9 mA h g^{-1}, which is higher than the theoretical capacity (1007 mA h g^{-1}). Two plateaus are observed during the first discharge. The peak located at 0.91 V corresponds to Li^+ metal insertion into Ag-Fe_2O_3 electrode, and the followed long stage at 0.79 V indicates that the reduction of Fe (III) to Fe (0) and the formation of SEI. When the discharged electrode is recharged to 3.0 V, a smooth voltage plateau is observed at 1.3 V, then the voltage profile has a sudden rise from 2.1 V to 3.0 V, which finally reaches a charge capacity as high as 726.9 mA h g^{-1}. The first initial coulombic efficiency is about 70.5%. This high initial irreversible loss may be due to the formation of SEI and structural change of electrode. Nevertheless, this initial coulombic efficiency of 70.5% is quite outstanding compared with some reports (no more than 50%)[42, 43]. In subsequent second and third discharge voltage

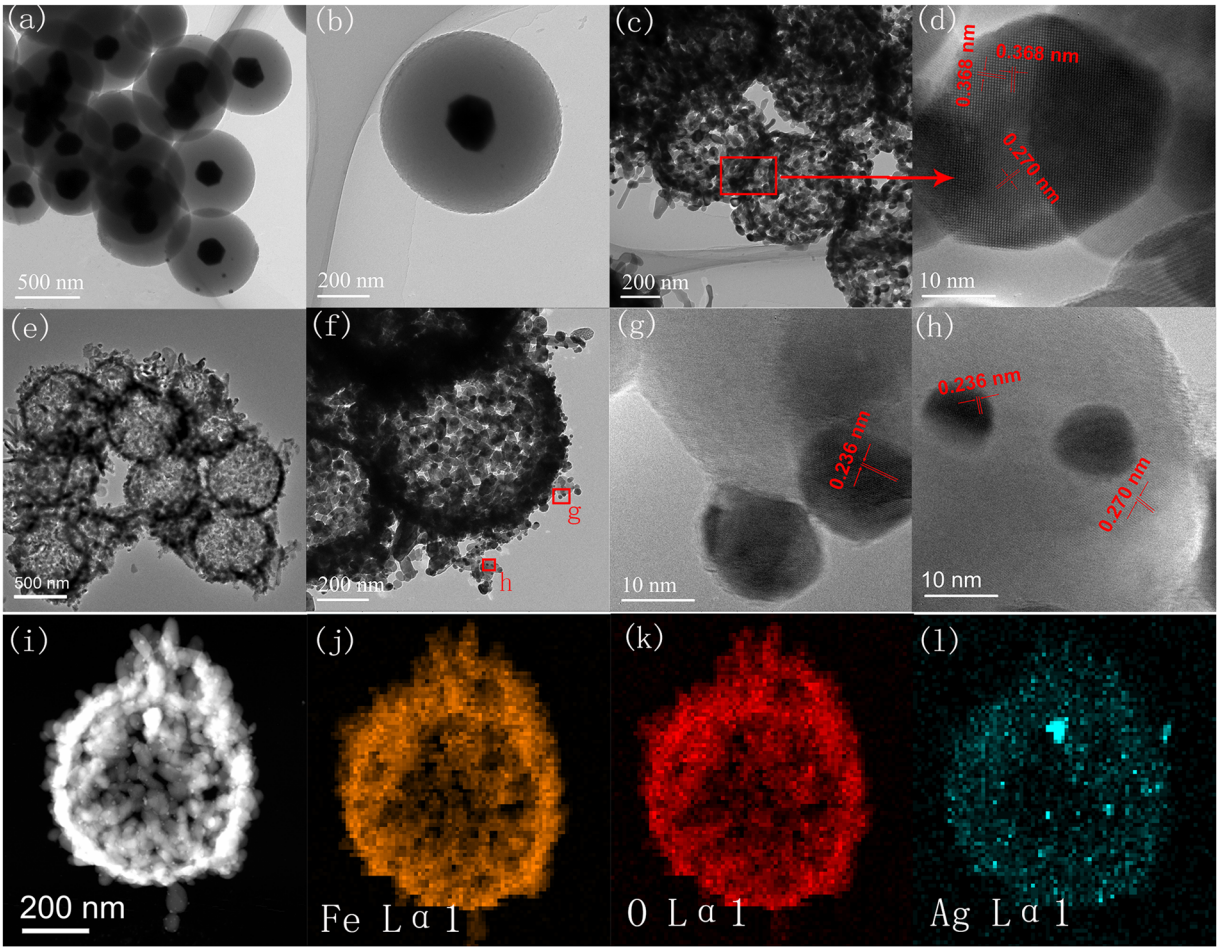

Figure 3. (**a**,**b**) TEM of Ag@C templates. (**c**) TEM of Fe_2O_3 nanospheres. (**d**) HRTEM of Fe_2O_3 nanospheres. (**e** and **f**) TEM of Ag-Fe_2O_3 composites. (**g** and **h**) HRTEM of Ag-Fe_2O_3 composites. (**i–l**) Phase mapping of Ag Lα1, Fe Lα1 and O Lα1.

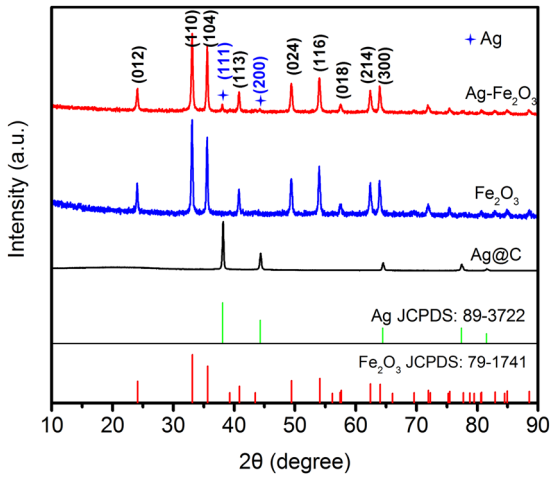

Figure 4. The XRD patterns of Ag@C templates, Fe_2O_3 nanospheres and Ag-Fe_2O_3 composites.

profiles, the plateaus rise to 1.05 V. The 60th discharge curve shows a slope at 0.98 V and the capacity increases to 947.8 mA h g^{-1}. Immediately after 60 cycles, a slight drop in specific capacity is recorded. The capacity decreases to 721.3 mA h g^{-1} at 125th cycle, which may be attributed to the crushing of the electrode. The plateau at 0.95 V of 125th cycle become shorter than previous cycles, which indicates a decreased capacity. Beyond 125th cycle,

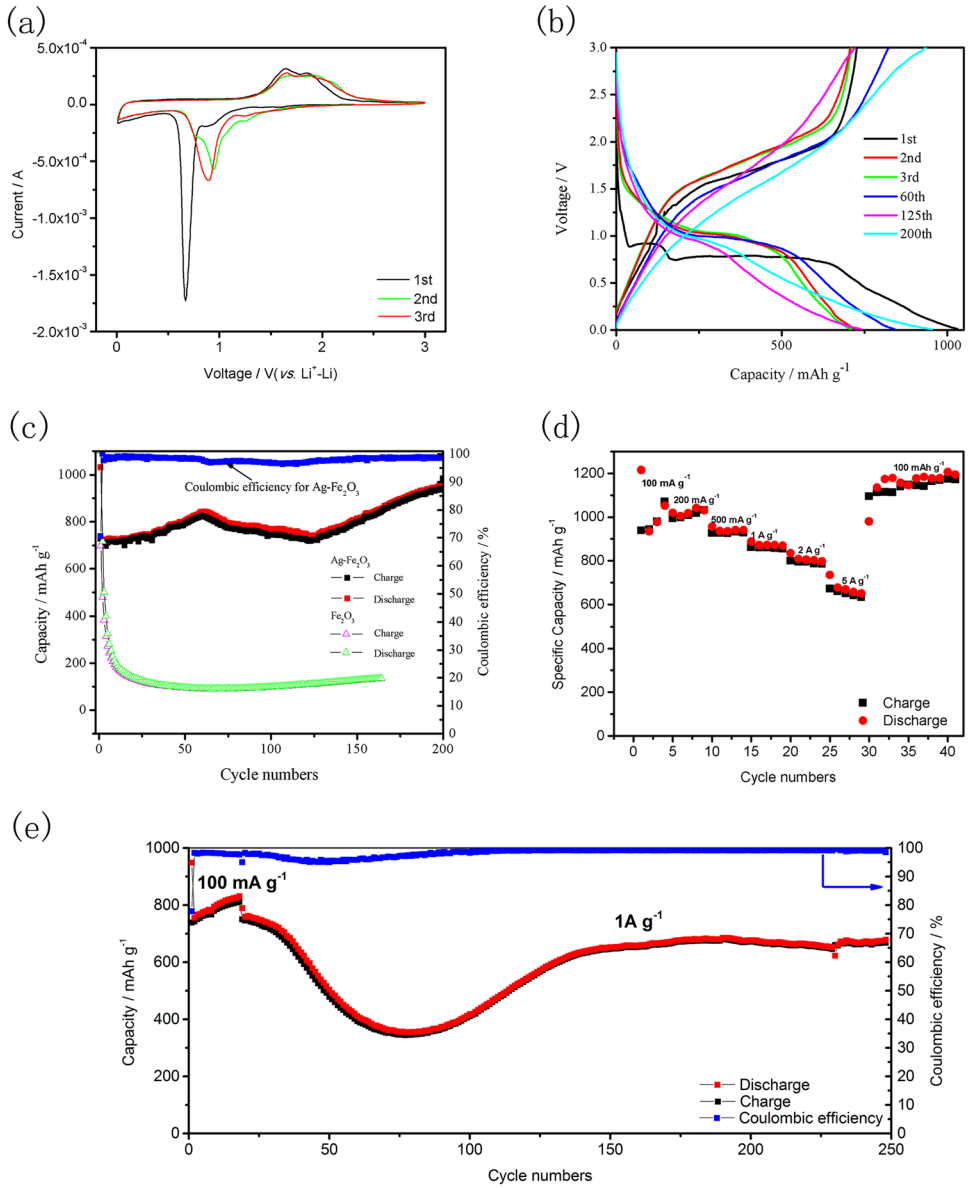

Figure 5. Electrochemical measurements (**a**) CV curves of Ag-Fe_2O_3 electrodes at a scan rate of 0.1 mV s^{-1} between 0.01 and 3.0 V, (**b**) Discharge and charge voltage profiles of Ag-Fe_2O_3 electrode at a current density of 100 mA g^{-1} for different cycles, (**c**) The cycling performance of Fe_2O_3 nanospheres and Ag-Fe_2O_3 composites electrode at 100 mA g^{-1}, (**d**) Rate capabilities of Ag-Fe_2O_3 composites electrode, (**e**) The cycling performance of Ag-Fe_2O_3 composites electrode at 1 A g^{-1}.

the capacity gradually increases to 953.2 mA h g^{-1} in the 200th cycle. The discharge curves' decay slow down with aging below 0.95 V from 125th to 200th cycles, which may be ascribed to the increased capacity. Such a low voltage hysteresis owing to faster ion migration rate and a reformative energy efficiency is absolutely necessary for the commercialized development of TMOs-based electrodes[44,45].

Figure 5(c) shows the cycling performance of the Ag-Fe_2O_3 anode which is tested at a current density of 0.1 A g^{-1}. For comparison, we also performs cycling experiment for the corresponding Fe_2O_3 anode. Worthy of nothing, the cycling process of Ag-Fe_2O_3 composites seems to undergo three different steps. Stage (A): from the 2nd cycle to 60th cycle, the anode of Ag-Fe_2O_3 exhibits a gradual enhancement of the lithium storage capacity. This increase in capacity may be due to the activation of the electrode and the formation of SEI during cycling. It takes several cycles to form stable SEI films on the discharge intermediates. These SEI films establish an intimate contact with connector which will improve the accessibility during the cycling. Stage (B): in the range of 60–125 cycle, the decomposition of electrode takes a predominant role[46,47]. Therefore, a slight drop in specific capacity is recorded. Stage (C): beyond the 125th cycle, one can see the curve shows an obvious gradual increase of the capacity. An anomalous monotonic increase in the discharge capacity is observed from the 125th (721.3 mA h g^{-1}) to 200th (953.2 mA h g^{-1}) cycle. Indeed this phenomenon (increasing of capacity) has also been reported previously[48]. The high-rate lithium-induced reactivation often occur in the hollow structure metal oxide electrode. A

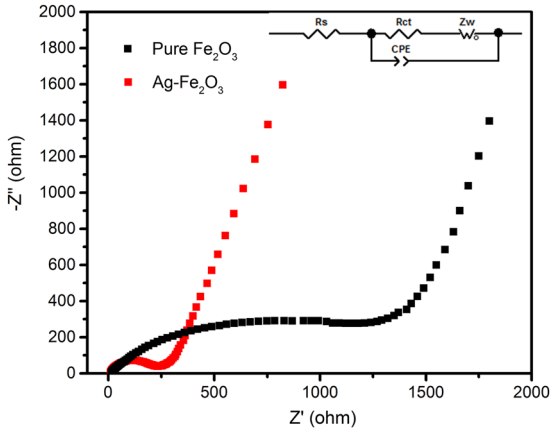

Figure 6. Nyquist plots of Fe_2O_3 and Ag-Fe_2O_3 composites electrode.

recent research commanded by Hu *et al.* provides more direct evidence on the origin of additional capacity[49]. The increasing capacity during cycling is attributed to the reversible formation and decomposition of an organic polymeric gel-like film from kinetic activation in the electrode, which can coat the active materials and provide extra lithium interfacial storage sites to enhance the mechanical cohesion. The outside SEI layer may be broken, peeled off and reformed, resulting in the thick and unstable SEI layer during the cycling with a declining capacity. When the structure refinement, a thin and stable SEI film gradually forms without splinter, then, the re-activated electrode will exhibit an excellent cycling stability in a long cycle. In general, the decomposition of electrode caused by volume change during cycling leading to capacity loss, while the reversible formation and decomposition of an organic polymeric gel-like film will result in increased capacity. For the purpose of exploring the role of Ag nanoparticles in improving the cycling properties of materials, the cycling performance of Fe_2O_3 nanospheres is also measured at a current density of 0.1 A g^{-1}. Fe_2O_3 anode delivers initial 1401 mA h g^{-1} discharge capacity and 697 mA h g^{-1} charge capacity with a coulombic efficiency of 49.8%, which is lower relative to the Ag-Fe_2O_3 composites. It shows about 80% coulombic efficiency at the first 5 cycles. After that the capacities of Fe_2O_3 maintain a stable value about 170 mA h g^{-1} during the following cycles (more than 150 cycles). Fe_2O_3 usually suffers from the problem of poor electronic conduction, which will cause serious polarization, resulting in instability during the cycling. In addition, particle pulverization caused by the great volume changes and the strong agglomeration during the charge and discharge process will all lead to a steep capacity fading[13,40,50]. As shown in Fig. S3(a and b), the sphere Fe_2O_3 structure is barely maintained after cycling, which also suggested large capacity fading. The result clearly indicates that the decoration of Ag nanoparticles significantly improves the electrochemical performance of the electrode. The ultra-small Ag nanoparticles evenly disperses on the surface of Fe_2O_3 nanospheres will protect the anode from pulverization during cycling, thereby enhancing the cycle stability of the electrode. In additional, the unusual cycle performance of the Ag-Fe_2O_3 composites electrode will also provide a case for future studies.

To further characterize the cycle performance of Ag-Fe_2O_3 anode, tests are performed at a current density of 0.1 A g^{-1} for 20 cycles, then increasing to 1 A g^{-1}. As shown in Fig. 5(e), Ag-Fe_2O_3 anode exhibits capacity of 678 mA h g^{-1} after 250 cycles at 1 A g^{-1}. Additionally, it is clear that the cycle at high current density is consistent with the trend at low current density except a slight difference in stage (B). This severe capacity decline trend may be ascribe to much serious electrode smash and irreversible reaction when the anode cycles at high current density. Metal oxides having a hollow structure can withstand a certain volume expansion at a low rate and during the first cycle. However, when cycling at a high-rate and longer cycles, the anode still subjected to severe mechanical degradation owe to the drastic volume changes inherently along with the conversion reaction.

A higher rate performance of LIBs electrode is particularly crucial, especially for high power density applications such as electric vehicles. Figure 5(d) shows the rate performance of the Ag-Fe_2O_3 hollow nanospheres at different current densities. Benefiting from the modification of Ag nanoparticles and hollow structures, the composites anode exhibits an excellent rate capability. When cycling at the current densities of 0.1, 0.2, 0.5,1, 2 and 5 A g^{-1}, the electrode shows discharge capacities of 938.2, 1009.5, 925.7, 860.3, 794.0, and 650.8 mA h g^{-1}, respectively. In addition, a high capacity of 1113 mA h g^{-1} can be achieved quickly when the current density change from 5 A g^{-1} to 0.1 A g^{-1}. Such a remarkable result obtained from Ag-Fe_2O_3 electrode is better than most Fe_2O_3-based electrodes previously reported, involving Fe_2O_3/CNT, Fe_2O_3/GF and Fe_2O_3-carbon composites[51–54]. For comparison, the rate performance of Fe_2O_3 nanospheres is showed in Fig. S2(b). The specific capacity decline seriously with increasing current densities, suggesting that Ag nanoparticle incorporation and hollow structure have a significant effect on improving rate performance.

The electrochemical impedance spectra (EIS) of Fe_2O_3 and Ag-Fe_2O_3 electrode is conducted to demonstrate that the decoration of Ag nanoparticles can obviously improve the charge transfer kinetics, which are given in Fig. 6. The Nyquist plot consists of a semicircle at middle frequency and a sloped line at low frequency. The semicircle at middle frequency is associated with charge transfer resistance (*R*ct). Ohmic resistance (*R*s) is related to the contact resistance between the active material and current collector. The sloped line at low frequency range is influenced by ion diffusion (*Z*w). The Constant Phase Element (CPE) is the physical quantity used to describe the

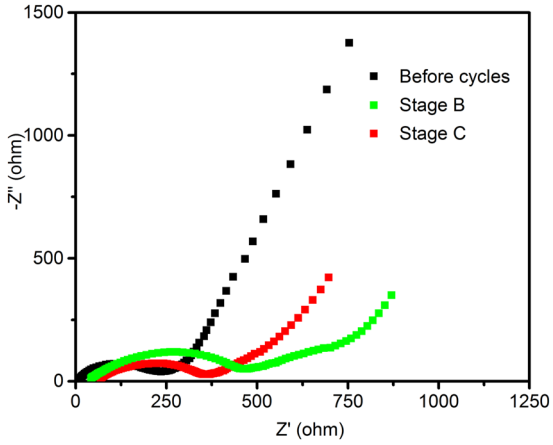

Figure 7. Nyquist plots of Ag-Fe_2O_3 composites electrode during stage (B) and stage (C) cycles.

deviation of the parameters of capacitor C, which depending on the nature of the system being investigated. The Nyquist plots for Ag-Fe_2O_3 composites possesses much smaller diameters of the semicircles than that of the pure Fe_2O_3. Based on equivalent circuit, the *R*ct values of Ag-Fe_2O_3 and Fe_2O_3 are 230 Ω and 1500 Ω, respectively. The difference in *R*ct indicates that the decoration of Ag nanoparticles can significantly enhance the conductivity of the material and thus promotes the charge transfer kinetics.

Figure 7 exhibits the impedance analysis of Ag-Fe_2O_3 composites electrode in stage (B) and stage (C) cycles. The charge transport resistance characterized by the semicircle at medium frequencies of stage (B) (400 Ω) is higher than that in stage (C) (300 Ω), which is consistent with the cycle performance. Therefore, the capacity rise can be ascribed to the reversible formation of polymeric/gel-like layer and/or interfacial lithium storage. The EIS result is agree with the cycling process of Ag-Fe_2O_3 composites electrode is shown in Fig. 5(c).

We also carry out SEM characterization of Fe_2O_3 and Ag-Fe_2O_3 composites electrode after 200 cycles (Fig. S3). Spherical Fe_2O_3 is barely found after cycling, and they become aggregated as shown in Fig. S3(a and b). On the contrary, the spherical structure of Ag-Fe_2O_3 composites is almost maintained after cycling as shown in Fig. S3(c), and even a number of hollow spheres exist as shown in Fig. S3(d). Therefore, uniform distribution of Ag nanoparticles on the surface of Fe_2O_3 nanospheres will benefit to the cycle stability of Ag-Fe_2O_3 nanocomposite electrode.

Conclusion

In summary, a hollow structure of Ag-Fe_2O_3 composites was synthesized by using Ag@C core-shell matrix as sacrificial templates and subsequent calcining process. In virtue of its hollow structure and the decoration of Ag nanoparticles over Fe_2O_3 nanospheres, the composites exhibited an improved cycling performance (~ 953.2 mA h g^{-1} at 100 mA g^{-1} after 200 cycles and 678 mA h g^{-1} at 1 A g^{-1} after 250 cycles). The Ag-Fe_2O_3 electrode also exhibited an extraordinary high-rate performance (~ 650.8 mA h g^{-1} at 5 A g^{-1}). Hence, this work showed that exploring of Fe_2O_3 composites might open venues for the practical applications of TMOs anodes in the next-generation of high-performance Li-ion batteries.

Methods

Preparation of Ag@C and Carbon spheres templates. All the reagents in the experiment were analytical grade and used without further purification.

Ag@C templates were synthesized by a modified hydrothermal method[55]. 30 mL of 10 mM $AgNO_3$ aqueous solution was added into 20 mL of 1 M glucose solution. After continual stirring for 30 min, the mixture was transferred to a 100 mL Teflon-lined autoclave and maintained at 180 °C for 6 h. After the autoclave naturally cooled down to the room temperature, the products were washed by water and ethanol respectively till the upper liquid become clear after centrifugation. Finally, the resulting products were oven-dried at 80 °C for 10 h. Furthermore, we also prepared carbon spheres in the same manner without addition of $AgNO_3$.

Preparation of Ag-Fe_2O_3 composites. 0.08 g of as-prepared Ag@C templates were dispersed in 50 mL deionized water. After ultrasonication for 30 min, 0.278 g of $FeSO_4{\cdot}7H_2O$ and 0.3 g of sodium acetate (NaAc) were added into the solution. Subsequently, the solution was stirred vigorously for 24 h at room temperature. Then, the resultant composites were purified by repeated centrifugation and dispersion cycle, and finally dried at 80 °C for 10 h. The final products of Ag-Fe_2O_3 composites were placed into the muffle furnace and calcined at 600 °C for 2 h in air. For comparison, we also synthesized Fe_2O_3 nanospheres using the as-prepared carbon templates with a similar procedure.

Materials characterization. Morphology and chemical compositions of the samples were characterized using scanning electron microscope (SEM, Zeiss SUPRA 55) equipped with an energy dispersive X-ray Spectroscopy (EDS, Oxford), transmission electron microscopy (TEM, JEOL JEM 2100) and high resolution transmission electron microscopy (HRTEM, JEOL JEM 2100), X-ray diffraction (XRD, Rigaku Ultima IV) were recorded on a Panalytical X-pert diffracto meter with Cu Kα irradiation.

Electrochemical measurements. The electrochemical measurements were characterized using CR2025-type coin cells. Pure lithium foils were used as the counter and reference electrodes. The active materials were mixed with carboxyl methyl cellulose and carbon black in a weight ratio of 80:10:10. The mixture was pressed onto copper foil and dried under vacuum at 100 °C for 10 h. The active material loading of the electrodes was about 0.8–1 $mg{\cdot}cm^{-2}$. The coin-cell was assembled in an argon-filled glove box with oxygen contents less than 0.5 ppm. The electrolyte was 1 M $LiPF_6$ in a mixture of EC, EMC, DMC (1:1:1, in v:v:v). A Celgard 2400 microporous polypropylene membrane was used as a separator. The cyclic voltammogram (CV) was performed by using a CHI 660E electrochemical workstation (Shanghai Chenhua Instrument Co., China) in the potential range of 0.01–3.0 V *vs*. Li/Li^+ at a scan rate of 0.1 $mV\,s^{-1}$. The electrochemical impedance spectroscopy (EIS) technique was measured at open circuit potential in a frequency range from 10^{-2} Hz to 10^5 Hz.

Data availability. All datasets generated or analysed during this study are included in this published article and its Supplementary Information files.

References

1. Xie, X. Q. *et al*. MoS_2 nanosheets vertically aligned on carbon paper: A freestanding electrode for highly reversible sodium-ion batteries. *Adv. Energy Mater.* **6**, 1502161–1502169 (2016).
2. Yuan, C. Z., Li, J. Y., Hou, L. R., Zhang, L. H. & Zhang, X. G. Template-free fabrication of mesoporous hollow $ZnMn_2O_4$ submicrospheres with enhanced lithium storage capability towards high-performance Li-ion batteries. *Part. Part. Syst. Char.* **31**, 657–663 (2014).
3. Gao, G. X., Yu, L., Wu, H. B. & Lou, X. W. Hierarchical tubular structures constructed by carbon-coated α-Fe_2O_3 nanorods for highly reversible lithium storage. *Small* **10**, 1741–1745 (2014).
4. Zhang, N., Zhao, Q., Han, X. P., Yang, J. G. & Chen, J. Pitaya-like Sn@C nanocomposites as high-rate and long-life anode for lithium-ion batteries. *Nanoscale* **6**, 2827–2832 (2014).
5. Poizot, P., Laruelle, S., Grugeon, S., Dupont, L. & Tarascon, J. M. Nano-sized transition-metal oxides as negative-electrode materials for lithium-ion batteries. *Nature* **407**, 496–499 (2000).
6. Gu, X. *et al*. Coaxial MnO/N-doped carbon nanorods for advanced lithium-ion battery anodes. *J. Mater. Chem. A* **3**, 1037–1041 (2015).
7. Wen, W., Wu, J. M. & Cao, M. H. Facile synthesis of a mesoporous Co_3O_4 network for Li-storage via thermal decomposition of an amorphous metal complex. *Nanoscale* **6**, 12476–12481 (2014).
8. Li, L., Raji, A. R. & Tour, J. M. Graphene-wrapped MnO_2-graphene nanoribbons as anode materials for high-performance lithium ion batteries. *Adv. Mater.* **25**, 6298–6302 (2013).
9. Lou, X. W., Deng, D., Lee, J. Y., Feng, J. & Archer, L. A. Self-supported formation of needlelike Co_3O_4 nanotubes and their application as lithium-ion battery electrodes. *Adv. Mater.* **20**, 258–262 (2008).
10. Huang, X. L. *et al*. Homogeneous CoO on graphene for binder-free and ultralong-life lithium ion batteries. *Adv. Funct. Mater.* **23**, 4345–4353 (2013).
11. Zhang, L., Wu, H. B., Madhavi, S., Hng, H. H. & Lou, X. W. Formation of Fe_2O_3 microboxes with hierarchical shell structures from metal-organic frameworks and their lithium storage properties. *J. Am. Chem. Soc.* **134**, 17388–17391 (2012).
12. Wang, B., Chen, J. S., Wu, H. B., Wang, Z. Y. & Lou, X. W. Quasiemulsion-templated formation of α-Fe_2O_3 hollow spheres with enhanced lithium storage properties. *J. Am. Chem. Soc.* **133**, 17146–17148 (2011).
13. Chen, M. H. *et al*. Porous α-Fe_2O_3 nanorods supported on carbon nanotubes-graphene foam as superior anode for lithium ion batteries. *Nano Energy* **9**, 364–372 (2014).
14. Chen, J., Xu, L. N., Li, W. Y. & Gou, X. L. α-Fe_2O_3 nanotubes in gas sensor and lithium-ion battery applications. *Adv. Mater.* **17**, 582–586 (2005).
15. Hao, S. J. *et al*. Phase transition of hollow-porous α-Fe_2O_3 microsphere based anodes for lithium ion batteries during high rate cycling. *J. Mater. Chem. A* **4**, 16569–16575 (2016).
16. Wang, Z. Y., Luan, D. Y., Madhavi, S., Hu, Y. & Lou, X. W. Assembling carbon-coated α-Fe_2O_3 hollow nanohorns on the CNT backbone for superior lithium storage capability. *Energy Environ. Sci.* **5**, 5252–5256 (2012).
17. Ye, F. *et al*. Engineering a hierarchical hollow hematite nanostructure for lithium storage. *J. Mater. Chem. A* **4**, 14687–14692 (2016).
18. Zhang, L., Wu, H. B. & Lou, X. W. Iron-oxide-based advanced anode materials for lithium-ion batteries. *Adv. Energy Mater.* **4**, 1300958–1300969 (2014).
19. Lei, D. N. *et al*. α-Fe_2O_3 nanowall arrays: hydrothermal preparation, growth mechanism and excellent rate performances for lithium ion batteries. *Nanoscale* **4**, 3422–3426 (2012).
20. Zhou, X. S., Yu, L. & Lou, X. W. Nanowire-templated formation of SnO_2/carbon nanotubes with enhanced lithium storage properties. *Nanoscale* **8**, 8384–8389 (2016).
21. Chen, Y. M., Yu, L. & Lou, X. W. Hierarchical tubular structures composed of Co_3O_4 hollow nanoparticles and carbon nanotubes for lithium storage. *Angew. Chem. Int. Ed.* **55**, 5990–5993 (2016).
22. Chen, J. F., Ru, Q., Mo, Y. D., Hu, S. J. & Hou, X. H. Design and synthesis of hollow $NiCo_2O_4$ nanoboxes as anodes for lithium-ion and sodium-ion batteries. *Phys. Chem. Chem. Phys.* **18**, 18949–18957 (2016).
23. Wang, S. H. *et al*. Nanoparticle cookies derived from metal-organic frameworks: controlled synthesis and application in anode materials for lithium-ion batteries. *Small* **12**, 2365–2375 (2016).
24. Jiang, H. *et al*. Rational design of MnO/carbon nanopeapods with internal void space for high-rate and long-life Li-ion batteries. *ACS Nano* **8**, 6038–6046 (2014).
25. Wang, Y. G., Li, H. Q., He, P., Hosono, E. & Zhou, H. S. Nano active materials for lithium-ion batteries. *Nanoscale* **2**, 1294–1305 (2010).
26. Han, F. *et al*. Nanoengineered polypyrrole-coated Fe_2O_3@C multifunctional composites with an improved cycle stability as lithium-ion anodes. *Adv. Funct. Mater.* **23**, 1692–1700 (2013).
27. Nam, K. T. *et al*. Virus-enabled synthesis and assembly of nanowires for lithium ion battery electrodes. *Science* **312**, 885–888 (2006).
28. Kim, J. *et al*. Controlled Ag-driven superior rate-capability of $Li_4Ti_5O_{12}$ anodes for lithium rechargeable batteries. *Nano Res.* **6**, 365–372 (2013).
29. Nam, S. H. *et al*. Ag or Au Nanoparticle-embedded one-dimensional composite TiO_2 nanofibers prepared via electrospinning for use in lithium-ion batteries. *ACS Appl. Mater. & Inter.* **2**, 2046–2052 (2010).
30. Steinhart, M. *et al*. Polymer nanotubes by wetting of ordered porous templares. *Science* **296**, 1997 (2002).
31. Lou, X. W., Li, C. M. & Archer, L. A. Designed synthesis of coaxial SnO_2@carbon hollow nanospheres for highly reversible lithium storage. *Adv. Mater.* **21**, 2536–2539 (2009).
32. Pei, F. *et al*. From hollow carbon spheres to N-doped hollow porous carbon bowls: rational design of hollow carbon host for Li-S batteries. *Adv. Energy Mater.* **6**, 1502539–1502547 (2016).
33. Chen, X. *et al*. Templating synthesis of SnO_2 nanotubes loaded with Ag_2O nanoparticles and their enhanced gas sensing properties. *Adv. Funct. Mater.* **21**, 2049–2056 (2011).

34. Chen, W., Pan, X. L. & Bao, X. H. Tuning of redox properties of iron and iron oxides via encapsulation within carbon nanotubes. *J. Am. Chem. Soc.* **129**, 7421–7426 (2007).
35. Choi, J. H. *et al*. Multimodal biomedical imaging with asymmetric single-walled carbon nanotube/iron oxide nanoparticle complexes. *Nano Letters* **7**, 861–867 (2007).
36. Chernyshova, I. V., Hochella, M. F. & Madden, A. S. Size-dependent structural transformations of hematite nanoparticles. 1. *Phase transition. Phys. Chem. Chem. Phys.* **9**, 1736–1750 (2007).
37. Hassan, M. F., Rahman, M. M., Guo, Z. P., Chen, Z. X. & Liu, H. K. Solvent-assisted molten salt process: A new route to synthesise α-Fe_2O_3/C nanocomposite and its electrochemical performance in lithium-ion batteries. *Electrochim. Acta* **55**, 5006–5013 (2010).
38. Jubb, A. M. & Allen, H. C. Vibrational spectroscopic characterization of hematite, maghemite, and magnetite thin films produced by vapor deposition. *ACS Appl. Mater. & Inter.* **2**, 2804–2812 (2010).
39. Cao, K. Z. *et al*. 3D hierarchical porous α-Fe_2O_3 nanosheets for high-performance lithium-ion batteries. *Adv. Energy Mater.* **5**, 1401421–1401430 (2015).
40. Jiang, Y. Z. *et al*. Amorphous Fe_2O_3 as a high-capacity, high-rate and long-life anode material for lithium ion batteries. *Nano Energy* **4**, 23–30 (2014).
41. Kan, J. & Wang, Y. Large and fast reversible Li-ion storages in Fe_2O_3-graphene sheet-on-sheet sandwich-like nanocomposites. *Sci. Rep.* **3**, 3502–3512 (2013).
42. Zhou, G. M. *et al*. A nanosized Fe_2O_3 decorated single-walled carbon nanotube membrane as a high-performance flexible anode for lithium ion batteries. *J. Mater. Chem.* **22**, 17942–17946 (2012).
43. Zhu, J. X. *et al*. Facile synthesis of metal oxide/reduced graphene oxide hybrids with high lithium storage capacity and stable cyclability. *Nanoscale* **3**, 1084–1089 (2011).
44. Etacheri, V., Marom, R., Elazari, R., Salitra, G. & Aurbach, D. Challenges in the development of advanced Li-ion batteries: a review. *Energy Environ. Sci.* **4**, 3243–3262 (2011).
45. Taberna, P. L., Mitra, S., Poizot, P., Simon, P. & Tarascon, J. M. High rate capabilities Fe_3O_4-based Cu nano-architectured electrodes for lithium-ion battery applications. *Nat. Mater.* **5**, 567–573 (2006).
46. Xu, X. D., Cao, R. G., Jeong, S. Y. & Cho, J. Spindle-like mesoporous α-Fe_2O_3 anode material prepared from MOF template for high-rate lithium batteries. *Nano Letters* **12**, 4988–4991 (2012).
47. Reddy, M. V. *et al*. α-Fe_2O_3 Nanoflakes as an anode material for Li-Ion batteries. *Adv. Funct. Mater.* **17**, 2792–2799 (2007).
48. Yu, W. J., Hou, P. X., Li, F. & Liu, C. Improved electrochemical performance of Fe_2O_3 nanoparticles confined in carbon nanotubes. *J. Mater. Chem.* **22**, 13756–13763 (2012).
49. Hu, Y. Y. *et al*. Origin of additional capacities in metal oxide lithium-ion battery electrodes. *Nat. Mater.* **12**, 1130–1136 (2013).
50. Zhu, X. J., Zhu, Y. W., Murali, S., Stoller, M. D. & Ruoff, R. S. Nanostructured reduced graphene oxide/Fe_2O_3 composite as a high-performance anode material for lithium ion batteries. *ACS Nano* **5**, 3333–3338 (2011).
51. Jin, S. L. *et al*. Facile synthesis of hierarchically structured Fe_3O_4/carbon micro-flowers and their application to lithium-ion battery anodes. *J. Power Sources* **196**, 3887–3893 (2011).
52. Zou, Y. Q., Kan, J. & Wang, Y. Fe_2O_3-graphene rice-on-sheet nanocomposite for high and fast lithium ion storage. *J. Phys. Chem. C* **115**, 20747–20753 (2011).
53. Zhang, M. *et al*. A green and fast strategy for the scalable synthesis of Fe_2O_3/graphene with significantly enhanced Li-ion storage properties. *J. Mater. Chem.* **22**, 3868–3874 (2012).
54. Wang, J. *et al*. Controlled synthesis of α-FeOOH nanorods and their transformation to mesoporous α-Fe_2O_3, Fe_3O_4@C nanorods as anodes for lithium ion batteries. *RSC Adv.* **3**, 15316–15326 (2013).
55. Zhao, P. L. *et al*. Design of Ag@C@SnO_2@TiO_2 yolk-shell nanospheres with enhanced photoelectric properties for dye sensitized solar cells. *J. Power Sources* **318**, 49–56 (2016).

Acknowledgements

This work was partly supported by the National Natural Science Foundation of China (Grant no. 61574118), and the Key Project of Science and Technology Plan of Fujian Province (grant No. 2015H0038).

Author Contributions

X.L. and Q.L. contributed to conception and design of the experiment, analysis of the data and writing the manuscript. X.T. and H.L. carried out synthesis and characterization of the materials. X.P., J.Z. and P.N. carried out the measurement of electrochemical performance. All the authors contributed to discussion on the results and preparation of manuscript. All authors have given approval to the final version of the manuscript.

Additional Information

Supplementary information accompanies this paper at doi:10.1038/s41598-017-08773-6

Competing Interests: The authors declare that they have no competing interests.

Publisher's note: Springer Nature remains neutral with regard to jurisdictional claims in published maps and institutional affiliations.